Boundary-Layer Meteorology (2019) 173:143–164
https://doi.org/10.1007/s10546-019-00464-1

RESEARCH ARTICLE

Statistical Investigation of Flow Structures in Different Regimes of the Stable Boundary Layer

Nikki Vercauteren[1] · Vyacheslav Boyko[1] · Amandine Kaiser[1] · Danijel Belušić[2]

Received: 22 October 2018 / Accepted: 2 July 2019 / Published online: 16 July 2019

Abstract
A combination of methods originating from non-stationary time-series analysis is applied to two datasets of near-surface turbulence in order to gain insights on the non-stationary enhancement mechanism of intermittent turbulence in the stable atmospheric boundary layer (SBL). We identify regimes of SBL turbulence for which the range of time scales of turbulence and submeso motions, and hence their scale separation (or lack of separation), differs. Ubiquitous flow structures, or events, are extracted from the turbulence data in each flow regime. We relate flow regimes characterized by very stable stratification, but differing in the dynamical interactions and in the transport properties of different scales of motion, to a signature of flow structures thought to be submeso motions.

Keywords Boundary-layer regimes · Clustering · Detection of events · Scale interactions · Submeso-scale motions

1 Introduction

The representation of the stable boundary layer (SBL) presents ongoing challenges, and modelling challenges increase with increasing stability (Sandu et al. 2013). Among the more unknown situations is the small wind-speed scenario in which the turbulence is weak and does not show significant dependence on the stratification. In such weak-wind situations, turbulence typically is non-stationary and a spectrum of motions on the so-called submeso scales is found to bridge the scale gap between the largest turbulent scales and the mesoscale (Anfossi et al. 2005; Belušić and Güttler 2010; Mahrt 2014). Weak turbulence is found to be enhanced by these submeso motions (Sun et al. 2015; Mahrt and Thomas 2016; Cava et al. 2016). Better understanding of the non-stationary enhancement mechanism is a necessary step towards improved SBL turbulence parametrization.

Recent approaches focus on distinguishing flow regimes in which turbulence behaves differently. Based on observations, Sun et al. (2012) identified a height dependent wind-

✉ Nikki Vercauteren
vercauteren@math.fu-berlin.de

[1] FB Mathematik und Informatik, Freie Universität Berlin, Arnimallee 6, 14195 Berlin, Germany

[2] Swedish Meteorological and Hydrological Institute (SMHI), 60176 Norrköping, Sweden

speed threshold that separates a regime in which the turbulence intensity increases slowly with increasing wind speed from a regime where the turbulence intensity increases rapidly with the wind speed. The weak turbulence, strongly stable regime is found to include cases where local shear-generated eddies are too small to interact with the ground and turbulence is no longer related to the bulk shear. Theoretical results also predict the appearance of two regimes based on the hypothesis that continuous turbulence requires the turbulence heat flux to balance the surface energy demand resulting from radiative cooling (van de Wiel et al. 2012a, b, 2017). A radiative heat loss that is greater than the maximum turbulent heat flux that can be supported by the flow with a given wind profile leads to the cessation of turbulence (van de Wiel et al. 2012a). This concept is used by van Hooijdonk et al. (2015) to show that the shear over a given layer thickness can predict SBL regimes when ensemble averaging of field observations is considered.

The very stable regime is, however, more likely to be dominated by apparently random, submeso-scale flow accelerations that generate local turbulence and lead to highly non-stationary flows (Acevedo et al. 2015). Such local flow accelerations have been revealed by released fog elements and by fine-scale spatially-distributed temperature measurements using fibre-optic distributed temperature sensing (Zeeman et al. 2014). The spatial observations highlighted transient temperature structures on the scales of metres for which the flow direction and velocity could be quantified. Numerical studies have shown that finite perturbations imposed on the flow after the cessation of turbulence suffice to act as a regenerating mechanism for turbulence (Donda et al. 2015). Donda et al. (2015) further found a strong sensitivity of the turbulence recovery to the timing and amplitude of added perturbations, thereby motivating the need for better characterization of submeso-scale motions and their effect on turbulence. Statistical analyses of the hydrodynamical equilibrium properties of the SBL flow revealed that the very stable regime is prone to long-term memory effects in the turbulence dynamics, suggesting a dynamically unstable flow (Nevo et al. 2017). The long-term memory effects can be related to submeso-scale motions that can propagate for some time in very stable flow regimes due to weak turbulent mixing. Such memory properties in the observed turbulent variables suggest that very stable flow regimes need to be represented by high-order closure models or stochastic processes (Nevo et al. 2017). A statistical characterization of submeso-scale flow structures and their transport properties would greatly help in defining such a stochastic process.

Despite numerous case studies highlighting the local shear generation of turbulence due to flow accelerations connected to submeso motions (Sun et al. 2004; Román Cascón et al. 2015; Mortarini et al. 2017), the general understanding of non-turbulent motions on submeso scales remains limited. Analyses of the propagation direction of submeso motions reveal no tendency to follow the mean wind direction (Lang et al. 2018) and highlight the difficulty of understanding the origin of such features of the flow. To extend case studies to more general observations, Kang et al. (2014) developed a method of extracting non-stationary motions from turbulent time series, regardless of the physical origin of the flow motions. Non-stationary flow structures deduced from SBL data were subsequently categorized into three classes with similar characteristics (Kang et al. 2015). The smoothest, wave-like structures were typically associated with higher wind speeds, active turbulence, and weak stability. The two other classes associated with higher stratification were found to have predominantly sharp structures with one including step-like structures that were attributed to microfronts.

To further investigate the local shear generation of eddies, Vercauteren and Klein (2015) followed a data-driven approach to identify regimes based on the relationship between turbulence and local wind variations on the submeso scales. The regime identification was based on the finite element, bounded variation, vector autoregressive factor models (FEM-BV-VARX)

Table 1 Site characteristics

Site	σ_w [m s^{-1}]	σ_w/V	V [m s^{-1}]	$\hat{V}$ [m s^{-1}]	$\hat{V}/V > 1$ [%]	σ^2_{vM}
SnoHATS	0.18	0.09	2.68	0.70	4.6	0.72
FLOSSII	0.31	0.06	5.26	0.74	10.18	0.35

Averaged values of the 30-min records for: the standard deviation of the vertical velocity fluctuations σ_w, the wind speed V, the submeso-scale wind speed $\hat{V}$ (defined formally in Sect. 3.1), the percentage of the time where the submeso-scale wind speed is greater than the speed of the 30-min averaged wind vector, and the submeso cross-stream velocity variance σ^2_{vM} (defined formally in Vickers and Mahrt 2007, Eq. 1). The average include all instruments at the site

clustering procedure (Horenko 2010; O'Kane et al. 2016), which allows to explicitly consider external factors influencing the dynamics of the variable of interest in the classification scheme. The automatic procedure was developed to isolate periods in which turbulence is related to local flow accelerations due to propagating non-turbulent motions on the submeso scales. Further analysis of one dataset revealed that one of two identified types of submeso-influenced regimes gathered cases in which a scale gap separated the smallest submeso scales from the largest turbulence scale. In the second such regime, submeso scales and turbulent scales seemed to overlap (Vercauteren et al. 2016). Based on the classification of submeso-influenced flow regimes, the present study attempts to characterize the statistics of submeso motions that occur in flow regimes characterized by different dynamical activities of submeso and turbulent scales of motion. The extraction of submeso motions is based on the turbulent event detection (TED) method proposed by Kang et al. (2015). The questions that are addressed are the following: is there a preferred type of submeso motion that interacts with turbulence? And does the frequency and type of submeso motions change depending on the regimes of SBL turbulence?

2 Data

Our study is based on sonic anemometer measurements from the Snow Horizontal Array Turbulence Study (SnoHATS, Bou-Zeid et al. 2010) and from the Fluxes over Snow Surfaces II (FLOSSII, Mahrt 2010) datasets. The SnoHATS dataset was collected over a large flat glacier on top of a mountain range, while the FLOSSII dataset was collected over a locally flat basin between two mountain ranges and includes several snow-covered periods. Some indicators of turbulence and submeso-scale activity are given for both sites in Table 1.

2.1 SnoHATS

The data were collected over the Plaine Morte Glacier in the Swiss Alps from February to April 2006, at 2750 m elevation (Bou-Zeid et al. 2010, data collected by the EFLUM laboratory at EPFL). The large flat glacier ensures long periods of stable stratification, and measurements were taken at a height varying between 2.82 m and 0.62 m, depending on snow accumulation. The set-up, shown in Fig. 1, consists of two vertically-separated horizontal arrays of sonic anemometers, with a total of 12 sonic anemometers (Campbell Scientific, model CSAT3). The vertical separation between the upper and lower array is 0.77 m (0.82 m after March 17), while the horizontal separation between the instruments is 0.80 m. The data analysis was restricted to wind directions within a $\pm 60°$ angle relative to the streamwise sonic

Fig. 1 Set-up of the SnoHATS field campaign. Left: Side view with the 12 instruments. Right: View in the direction of measurements showing the 1500 m fetch

axis (corresponding to easterly winds), ensuring that data are not affected by the structure supporting the instruments. The resulting fetch consists of 1500 m of flat snow. After removing data with unfavourable flow angles (outside the selected $\pm 60°$ range) or low quality (snow-covered sonics, power outages), about 15 non-continuous days of data remained available for analysis. The 20-Hz raw data were preprocessed and conditioned using axis rotations to correct for the yaw and pitch misalignments of the sonics, linear detrending, and density correction.

2.2 FLOSSII

The data were collected from 20 November 2002 to 4 April 2003 over a locally flat surface south of Walden, Colorado, USA, in the Arapaho National Wildlife Refuge. The surface consists of matted grass with brush upwind over a distance of about 100 m, with the grass often covered by a thin snow layer during the field program. A tower allowed measurements at 1, 2, 5, 10, 15, 20 and 30 m with Campbell CSAT3 sonic anemometers, and the data from the second level (2 m) are used to identify flow regimes, extract and characterize events. The choice of the 2-m level is made to be similar to the SnoHATS data, as well as to be high enough above the ground to avoid dissipation of structures by small-scale turbulence near the surface. It also ensures that the measurements remain within the boundary layer, which can be very shallow in strongly stable conditions. Investigations of the height dependence of flow regimes is left for future work. Here, instead, the transport characteristics of different scales of motion are analyzed at several heights assuming that the regime affiliation is the same for all heights. The dataset was quality controlled and segments of instrument problems and meteorologically anomalous values were eliminated (Larry Mahrt, personal communication, 2018). We restrict the analysis to night-time data, taken between 1800 and 0700 local time. Flow-regime identification based on the FEM-BV-VARX clustering methodology (see Sect. 3.1) ideally requires continuous data, however the dataset consists of continuous night-time data separated by gaps during the day. In order to maximize continuity of the night-time dataset, periods with data gaps corresponding to more than 80 min over a single night (12 nights), as well as nights with flow through the measurement tower for periods longer than 5 min (51 nights), were removed from the analysis. The resulting 68 nights left for analysis have data gaps shorter than 1 min and are deemed uncontaminated. The short gaps are linearly interpolated. The 60-Hz raw data are double rotated into the mean wind direction based on 30-min averages.

3 Methods

Our analyses of flow structures in the SBL are based on two complementary methods. In a first step, flow regimes are identified based on the intensity of turbulent velocity fluctuations and their modulation by a submeso-scale wind velocity. The identification uses a data-clustering methodology based on a finite element, bounded variation, vector autoregressive factor method (FEM-BV-VARX) introduced by Horenko (Horenko 2010; O'Kane et al. 2013). We hypothesise that the turbulence is occasionally modulated by the wind variability on submeso scales (typically in weak flow, strongly stable situations) and our goal is to automatically detect periods in which the submeso-scale wind speed influences the turbulence (Vercauteren and Klein 2015). In the second step, we apply the turbulent event detection method introduced by Kang et al. (2014, 2015) to detect events in noisy time series. The types of turbulent event occurring are analyzed in each of the FEM-BV-VARX identified flow regime separately, thus giving an indication of the type of submeso motions occurring in each of the flow regimes detected based on scale-interaction properties.

3.1 Classification of Flow Regimes

We briefly review the mathematical framework used to classify the flow regimes in terms of their scale-interaction properties. For full details of the mathematical framework, we refer to Horenko (2010), while further details on its application to SBL flow-regime classification can be found in Vercauteren and Klein (2015).

The FEM-BV-VARX method relates an observed variable of interest at a discrete time t to its past history, and to the past history of external forcing variables. The classification of SBL flow regimes is based on the hypothesis that in some flow regimes, turbulence may be modulated to a large extent by submeso-scale motions. Those flow regimes are expected to correspond to weak-wind, very stable periods. Our classification goal is to separate cases during which the time evolution of turbulence is modulated by the time evolution of the submeso-scale wind speed from cases during which the response of turbulence to forcing by submeso scales is different or less apparent. More specifically, we assume that the evolution in time of the vertical velocity fluctuations $\sigma_w = \sqrt{\overline{w'w'}}$ (where the overbar denotes an averaging period of 1 min and the prime denotes deviations from the average) can be approximated by several locally stationary statistical processes that are influenced by the submeso-scale horizontal wind speed $\hat{V}$, defined on scales between 1 and 30 min. The submeso-scale wind speed is defined formally as

$$\hat{V} = \sqrt{\hat{u}^2 + \hat{v}^2}\,, \tag{1}$$

where $\hat{\phi} = \overline{\phi} - [\phi]$, the overbar denotes a 1-min averaging time, and the square brackets denote a 30-min averaging time, such that these fluctuations represent the deviations of the 1-min sub-record averages from the 30-min average. The definition of submeso scales is made because these are scales that typically correspond to non-turbulent motions in weak-wind SBL flows (Mahrt et al. 2012a). Furthermore, the choice of the 1-min averaging time for the vertical velocity variance is a compromise between minimizing the loss of flux by larger-scale turbulent motions in windy conditions and minimizing the contamination of the computed fluctuations by non-turbulent motions for weak-wind, more stable, conditions.

The statistical processes representing the time evolution of σ_w in the FEM-BV-VARX framework are vector autoregressive models with exogenous factors (VARX) and the submeso-scale wind speed $\hat{V}$ is considered as the exogenous factor. Our analyses show

that models that include an autoregressive part do not give any reproducible solutions to the clustering problem. Hence we restrict our search to models including only the exogenous part,

$$\sigma_{w;t} = \mu(t) + B_0(t)\hat{V}_t + \cdots + B_m(t)\hat{V}_{t-m\tau} + C(t)\epsilon_t, \tag{2}$$

where the process $\sigma_{w;t}$ is the time evolution of the 1-min vertical velocity variance measured at one location; the external factors $\hat{V}_t$ are the time evolution of the horizontal wind speed on scales between 1 and 30 min; $\epsilon_t : [0, T] \rightarrow \mathbb{R}^h (h \ll n)$ is a noise process with zero expectation, the parameters μ, B and C are time-dependent coefficients for the statistical process, m is the memory depth of the external factor that needs to be estimated, and τ is the discrete time increment (here 1 min). The number of statistical processes corresponds to the number of clusters; the assumption of local stationarity of the statistical process is enforced by setting a persistency parameter C_p, which defines the maximum allowed number of transitions between K different statistical processes (corresponding to K different values of the model coefficients in Eq. 2). The cluster states are indicated by a cluster affiliation function, which is calculated from the procedure. The assumption of local stationarity of the statistical process is equivalent to assuming that the dynamics consists of several persistent flow regimes. In other words, the characteristic fluctuation time scale of the data is assumed to be fast compared to the time scale at which switches between flow regimes occur. In each flow regime, an optimal process of the form given in Eq. 2 provides a representation of the statistical modulation of the dynamics of the vertical velocity variance by the submeso-scale wind speed. The reader is referred to Horenko (2010) for information regarding the minimization procedure used to solve the clustering problem, while more detailed explanations on the application of the classification scheme to SBL turbulence are given in Vercauteren and Klein (2015). User defined parameters and their choice are discussed in Sect. 4.1.

3.2 Turbulent Events Detection

The time-series analysis methodology for turbulent-event detection derived by Kang et al. (2014) aims at identifying non-stationary events or flow patterns in noisy time series. Instead of detecting signatures of known flow patterns in time series, the TED method detects flow structures as events that are significantly different from noise. In the context of time series resulting from turbulent quantities, the noise is taken as white and red noise. Indeed, statistical descriptions of turbulence as first suggested by Kolmogorov (1941) and Obukhov (1941) lead to the formulation of stochastic models for the turbulent observed variables such that, in the inertial subrange, Lagrangian velocities can be modelled using a Langevin equation (or Ornstein-Uhlenbeck process) with suitable drift and noise terms (Thomson 1987). In the particular case of stationary and isotropic turbulence, all components of the fluid particle velocity are statistically identical and the Langevin equation takes the following one-dimensional form (Pope 2000),

$$\mathrm{d}u = -\frac{u}{T}\mathrm{d}t + \sqrt{C_0\varepsilon}\,\mathrm{d}W\,, \tag{3}$$

where u is the statistical representation of one component of the fluid particle velocity (or that of a scalar turbulent variable), T is the Lagrangian decorrelation time scale, C_0 is a universal constant and ε is the the mean dissipation; $\mathrm{d}W$ are increments of a Wiener process. As shown in Faranda et al. (2014), this model, when discretized, is in fact equivalent to an autoregressive process of order one (AR(1)) process (also known as red noise),

$$u_t = \phi\, u_{t-1} + \psi_t\,, \tag{4}$$

where t is a discrete time label, $\phi = 1 - \Delta t/T$, and ψ_t represents independent variables, normally distributed.

In the SBL, gravity waves, transient drainage flows, and other flow structures on the submeso scale will typically superimpose on the turbulence or affect its intensity, thereby inducing non-stationarity and hence departures from the idealized inertial subrange Langevin model (3) or AR(1) process (4). The deviations of turbulent time series from AR(1) processes were in fact studied in Nevo et al. (2017) to investigate the hydrodynamical equilibrium properties of turbulence in different SBL flow regimes, showing that intermittent or strongly stable regimes exhibit long memory effects in the turbulence dynamics. The core idea of the TED method is also to analyze deviations from AR(1) processes: in a first step, sequential subsequences of the time series $x(t)$ of turbulent observed variables are analyzed using a sliding window of predefined length scale l. The q-th subsequence is thus

$$x_q(t) = \left\{x(t_q), \ldots x(t_{q+l-1})\right\}\,, \tag{5}$$

where $1 \leq q \leq (n - l + 1)$ and n is the length of the time series $x(t)$. Events are defined as subsequences that are significantly different from white noise or from an AR(1) process. In practice, an AR(1) process is fitted to each detrended subsequence $x_q(t)$ and a test is performed on the model residuals to see whether they are uncorrelated. If this is not the case (i.e. if the residuals are not white noise), then $x_q(t)$ is defined as a potential event. Additionally, non-stationary subsequences that exhibit a structural break are considered as potential events. Note that the noise process is not removed from the subsequence, meaning that the potential event consists of the raw subsequence.

The TED approach assumes that the typical duration of an event is known, but its form is unknown. In the context of detecting submeso motions, this is appropriate since submeso motions can take many different forms that are poorly known, but the typical duration of events is on the scale of minutes to an hour. A complementary approach to the detection of events in noisy time series is to assume that the form of events is known, while the duration is unknown. This approach is proposed in Lilly (2017) where wavelet elements embedded in noise detect isolated events of a known form. The reader is referred to Kang et al. (2014, 2015) for full details on the TED method. Time-scale considerations are discussed next.

3.3 Averaging Time Within the Turbulent Event Detection Approach

In the TED method, the length of the time window l has to be predefined. On the fastest scales, the signal is most likely purely turbulent, and block averaging on small-enough scales accelerates calculations without losing information on the submeso scales. The choice of scale for the block averages of the turbulent observed variables defines the time increments of the AR(1) process in Eq. 4. Hence the averaging scale should be chosen such that the increments fall within the range of scales of inertial turbulence. As shown by the extended multiresolution decomposition (MRD) analyses in Vercauteren et al. (2016), scales faster than approximately 5–10 s exhibit fluctuations characteristic of isotropic turbulence and block averaging within this time range represents an appropriate choice.

In order to have results comparable to the analyses of Kang et al. (2015), we thus consider their choice of block averages of 6 s and a window length of 120 points (12 min). As discussed in Kang et al. (2014), events can be detected on multiple overlapping windows, such that the maximal event length is not limited to one window length. The extended MRD results in Vercauteren et al. (2016) highlight non-turbulent fluctuations in the range of 50 s to 20–30

min, depending on the flow regime. The window length of 12 min, with possibilities of longer events through overlapping windows, is hence deemed appropriate.

For the analysis of multiple scales, according to Kang et al. (2014), keeping l constant and block averaging the time series to a desired scale leads to improved results. This is due to the fact that the test statistic applied for the white noise test depends on l, and keeping l constant returns consistent results for all scales. Tests varying the size of block averages between 1 and 15 s (while keeping $l = 120$ points for consistency) showed a large sensitivity of the event detection to the choice of scales, highlighting the difficulty of using automatic methods for analyses of submeso motions (Kaiser 2016). Block averaging on scales shorter than 3 s returned many short and insignificant events, while averaging on blocks longer than 9 s returned very few events. The range of scales between 4 and 8 s returned qualitatively consistent results. Acknowledging the sensitivity to the exact choice of an averaging time, we present our results using the aforementioned time scales—deemed physically appropriate by the MRD analyses—in the following section. Note that this averaging time scale is used only for the TED procedure, the FEM-BV-VARX clustering being based on 1-min averages as explained earlier.

4 Results

4.1 Parameters Selection for Flow Regime Classification

The FEM-BV-VARX framework is used to classify flow regimes in the SnoHATS and in the FLOSSII datasets. The turbulence data under consideration in Eq. 2 relates to the time evolution of the 1-min vertical velocity variance measured at one location, $\sigma_w(t)$; the external factor is the time evolution of the streamwise velocity component on scales between 1 min and 30 min at that location, $\hat{V}(t)$. For the SnoHATS dataset, this location corresponds to one of the 12 sonic anemometers (results showed little sensitivity to the choice of instrument). For the FLOSSII dataset, the location is chosen as the second level (2 m), corresponding to a height similar to that in the SnoHATS data.

User-defined parameters include the maximum memory depth m for the forcing variable, the number of clusters K and the persistency parameter C_p, which limits the number of transitions between the clusters. The maximum memory lag that we use in this model is determined by a priori calculation of the partial autocorrelation function for the variables σ_w and $\hat{V}$ (Brockwell and Davis 2002). The correlation between the time series decreases on average after a few minutes, and was set to $m = 3$ for the SnoHATS dataset and $m = 6$ in the FLOSSII dataset (based on the average obtained over 68 nights). To determine the optimum numbers for K and C_p, multiple models are fitted for varied values of the parameters K and C_p. The Akaike information criterion (AIC, see Brockwell and Davis 2002) was used in Vercauteren and Klein (2015) to select the optimal number of cluster states $K = 4$ and the persistency parameter $C_p = 20$ for the SnoHATS data.

For the FLOSSII dataset, however, the AIC exhibits asymptotic behaviour towards zero for all models in the investigated parameter space ($K = 2, 3, 4, 5, 7$ and $C_p = [2, 302]$) and cannot be used as a selection criterion. Instead, the optimal model parameters are selected as those that minimize the correlation between the signal σ_w and the model residuals ϵ_t, while maximizing the amount of variance of the signal explained by the model. Increasing the parameters beyond $K = 3$ and $C_p = 150$ does not reduce the correlation in the residuals and does not increase the modelled variance. Thus the choice of $K = 3$ and $C_p = 150$ is

considered as an optimal model. The amount of variance of $\sigma_w(t)$ explained by the VARX model in the three clusters is 0.8%, 3% and 9.5%.

Analysis of the model residuals in the three clusters, however, showed that the error distribution in the cluster corresponding to the largest explained variance of 9.5% was not Gaussian. This cluster gathers the smallest values of σ_w and has the most interaction between submeso scales and vertical velocity fluctuations and we wish to classify the dynamical interactions more accurately. Therefore, we select the time series in this specific cluster and classify it with the FEM-BV-VARX methodology further into two distinct clusters. This strategy leads to error distributions that are closer to normally distributed in the two subsequent clusters. Selecting only those periods of larger dynamical interactions between σ_w and $\hat{V}$ enables a second level clustering that differentiates the dynamical interactions between σ_w and $\hat{V}$ and not just the average intensity of the turbulent fluctuations.

The different performance of the AIC as a selection criterion can be explained by the different characteristics of both datasets in relation to the statistical model assumption. The VARX models to be fitted consist by assumption of an average value of σ_w ($\mu(t)$ in Eq. 2) and of the past history of $\hat{V}$. If the past history of $\hat{V}$ is unrelated to the dynamics of σ_w, as could be expected from weakly stable periods, the clustering of data will result mainly from classification of the mean value of σ_w. In this case of classification based on the mean value of σ_w, choosing the optimum based on standard information criteria resulted in an overfitted solution. The SnoHATS dataset includes a large number of strongly stable periods during which the modulation of σ_w by $\hat{V}$ is significant (see Table 2 and next paragraph), thus the statistical modelling assumption is appropriate, and selecting the optimal clustering result based on standard information criteria is sufficient. During FLOSSII, strongly stable periods were observed but strongly outnumbered by periods of stronger flow or cloud cover. In those weakly stable periods, the dynamics of σ_w is barely related to that of $\hat{V}$. The two-step procedure followed here enables the isolation of periods of low mean values of σ_w, and then to classify those periods according to the dynamical modulation of the signal by $\hat{V}$. The decision of classifying the FLOSSII data exhibiting modulation by $\hat{V}$ into two clusters (and not more) is arguably subjective, but the decision of a second level classification is based on analysis of the noise and thus on an objective criterion. We decided not to extend the second level of clustering to more flow regimes, partly for simplicity. Further analyses will highlight differences in the obtained flow regimes and the classification is deemed informative. Note that each dataset is thus classified in four distinct regimes, which do not necessarily correspond to the same flow types at the SnoHATS and FLOSSII sites. Hereafter, the flow regimes obtained at the SnoHATS site are denoted by S1–S4, and at the FLOSSII site by F1–F4. The regimes are numbered following increasing median stability of the flow.

The model coefficients fitted in each cluster give a quantitative indication of the scale interactions at both sites in each flow regime. The VARX model in Eq. 2 contains a total of six parameters for SnoHATS, and nine parameters for FLOSSII, where the difference is due to the different maximal memory depth m set from the analysis of the partial autocorrelation function: μ corresponds to the mean value of σ_w, while B_0 to B_3 (for SnoHATS) or B_0 to B_6 (for FLOSSII) are the weights associated with the past history of the external factor $\hat{V}$ and C is the weight associated with the noise part of the model. In order to compare the relative weight of the mean versus the external factor in each statistical model, we normalize each parameter by the mean value μ of the corresponding model. We then compute the norm $||\mathbf{B}_{Si}/\mu_{Si}||$ (resp. $||\mathbf{B}_{Fi}/\mu_{Fi}||$ for FLOSSII) of the vector $\left(B_0^{Si}/\mu_{Si}, \ldots, B_3^{Si}/\mu_{Si}\right)$ (resp. $\left(B_0^{Fi}/\mu_{Fi}, \ldots, B_6^{Fi}/\mu_{Fi}\right)$ for FLOSSII), where μ_{Si} and $\mathbf{B}_{Si}$ are associated with the model coefficients in cluster Si to estimate the relative weight of the external forcing compared to

Table 2 Statistical causality between the signal σ_w and the external factor $\hat{V}$ as quantified by the relative weights of the model coefficients in Eq. 2, in each cluster

Site	Flow regime	$\|\|\mathbf{B}_{Si}/\mu_{Si}\|\|$ or $\|\|\mathbf{B}_{Fi}/\mu_{Fi}\|\|$
SnoHATS	S1	0.11
SnoHATS	S2	0.22
SnoHATS	S3	0.92
SnoHATS	S4	2.20
FLOSSII	F1	0.04
FLOSSII	F2	0.04
FLOSSII	F3	0.11
FLOSSII	F4	0.29

The norm of the vector of weights associated to the submeso-scale wind velocity $(B_0, \ldots B_m)$ is normalized by the weight of the mean part in the model, μ, for each individual model or cluster

the mean in each statistical model. Note that, with this normalization, the weight of the mean is always 1. The values obtained for each flow regime at both sites are listed in Table 2. The increasing values for increasing stability denote that the more stable cases show a greater statistical causality between submeso scales of motion and turbulence. The method thus captures subtle differences in scale interactions between different regimes. The results also highlight that the FLOSSII data are characterized by less modulation of the turbulence by the submeso-scale wind speed than the SnoHATS data, reflecting the difficulty in obtaining an optimal number of clusters at FLOSSII based on our scale-interaction hypothesis.

Flow characteristics are given for each cluster in Table 3, with the gradient Richardson number

$$Ri = (g/\Theta_0)\frac{\partial\bar{\theta}/\partial z}{\left(\partial\bar{\mathbf{V}}/\partial z\right)^2}, \tag{6}$$

used for indicative assessment of the stability properties in each regime. In (6), g is the acceleration due to gravity, θ is the potential temperature (Θ_0 being the averaged one over the record), $\mathbf{V}$ is the wind vector, and the overline denotes a time average of 1 min. The vertical gradients are calculated using the averages of the upper and lower sensors for the SnoHATS data, and using the 1-m and 10-m levels for the FLOSSII data. The median and quartiles of Ri in each cluster (Table 3) show that weakly stable periods are separated from strongly stable periods by the FEM-BV-VARX procedure with, however, large overlaps in the distributions of Ri in the different clusters. Since the classification is based on the modulation of the turbulence by the submeso-scale wind speed, this separation (along with the statistical causality results in Table 2) strengthens the hypothesis that modulation of the turbulence by submeso motions differs between the weakly and very stable regimes. The overlap of distributions of Ri and their significant spread highlights the difficulty of defining a threshold based on Ri for distinguishing flow regimes. Especially in the most stable flow regimes, Ri values might be highly variable in time and may not be the right indicator of the turbulence level. Indeed, in the context of strong modulation by a constantly changing submeso-scale wind speed, the turbulence will likely not be in statistical equilibrium with the wind forcing, and thus Ri does not alone suffice to characterize the turbulence. Analyses of the anisotropy characteristics of turbulence in the FLOSSII dataset give further indication of a lack of statistical equilibrium of the turbulence in flow regimes F3 and F4 (Vercauteren et al. 2019).

Table 3 Flow characteristics in each flow regime

Site	Flow regime	Ri	$V\,(\mathrm{m\,s^{-1}})$	$\hat{V}\,(\mathrm{m\,s^{-1}})$	$\frac{\hat{V}}{V} > 1\,(\%)$
SnoHATS	S1	0.02 (0.01, 0.05)	5.6 (3.9, 7.1)	1.6 (1.0, 2.4)	7.8
SnoHATS	S2	0.12 (0.06, 0.23)	4.2 (3.2, 5.2)	0.8 (0.5, 1.2)	4.8
SnoHATS	S3	0.29 (0.10, 0.80)	2.1 (1.3, 3.0)	0.8 (0.5, 1.3)	12.8
SnoHATS	S4	0.67 (0.28, 1.76)	1.9 (1.1, 2.7)	0.4 (0.3, 0.7)	6.5
FLOSSII	F1	0.03 (0.02, 0.04)	9.0 (7.8, 10.3)	0.6 (0.3, 1.1)	0.2
FLOSSII	F2	0.07 (0.05, 0.10)	5.7 (4.8, 6.7)	0.4 (0.2, 0.8)	0.3
FLOSSII	F3	0.14 (0.10, 0.24)	3.6 (2.7, 4.4)	0.5 (0.2, 0.9)	5.5
FLOSSII	F4	0.58 (0.26, 1.55)	1.3 (0.7, 2.1)	0.4 (0.2, 0.8)	16.6

Richardson number, wind speed, submeso-scale wind speed (Median (first and third quartiles) given for each value), and the percentage of times where the submeso wind speed exceeds the wind speed. All values are based on 1-min averaged data

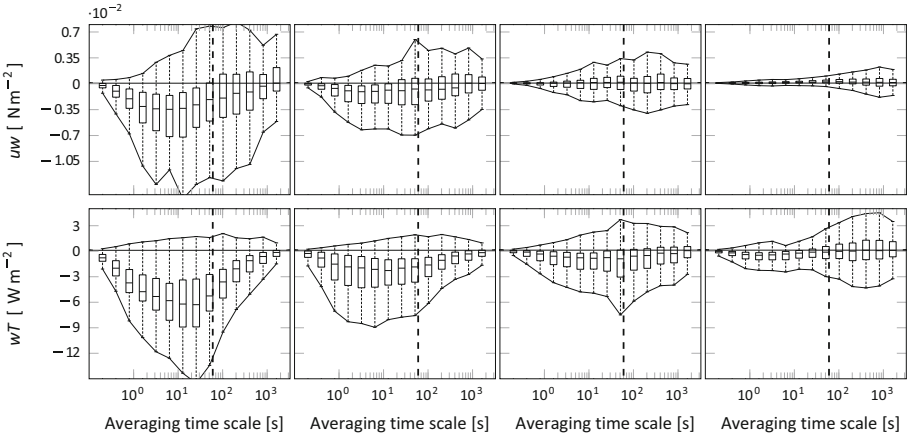

Fig. 2 MRD cospectra of the SnoHATS dataset. Top panels: momentum cospectra, bottom panels: heat cospectra. From left to right: regime S1–S4. The major dashed vertical lines in every panel mark the 1-min scale. Each panel contains box plots representing the distribution of the MRD flux on a corresponding scale. The boxes represent the 25th and 75th percentiles, and the whiskers across the scales are connected with a solid line. The horizontal line in each box shows the median. The statistics are calculated based on all 30-min periods within a flow regime. From S1 to S4, there are respectively 111, 148, 111 and 343 individual periods

4.2 Scale Interaction Properties

In each identified regime of near-surface SBL turbulence, the transport properties of different scales of motion are assessed using a multiresolution flux decomposition (MRD) (Vickers and Mahrt 2003). The scale-dependent transport properties are shown in Figs. 2, 3 and 4, based on MRD analyses of the heat and momentum fluxes. In each figure, boxplots show the median and quartiles of MRD fluxes calculated based on all sampled 30-min windows in each flow regime. The MRD cospectra of the SnoHATS data are shown in Fig. 2 for the flow regimes S1 to S4, and the MRD cospectra of the FLOSSII data are shown for heights of 2 m, 15 m and 30 m in Fig. 3 (for the sensible heat flux) and Fig. 4 (for the momentum flux) for the four classified flow regimes F1–F4 (from left to right). The dashed vertical

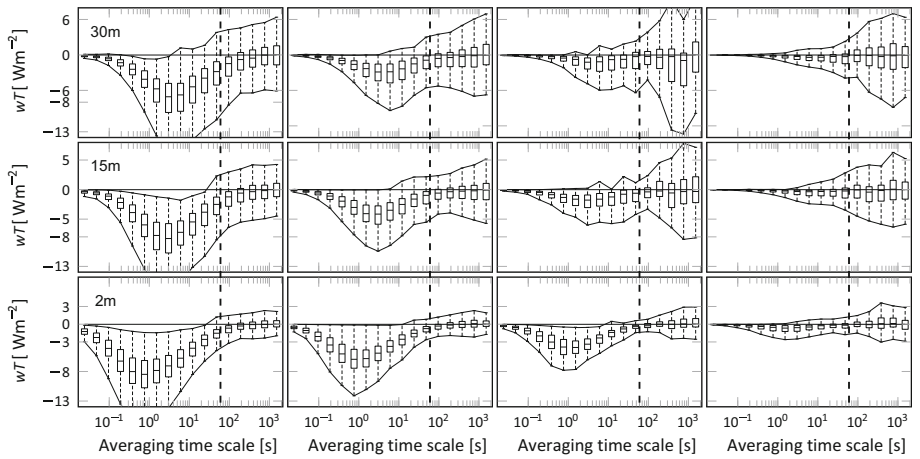

Fig. 3 MRD heat cospectra of the FLOSSII dataset. The top, middle and bottom rows correspond respectively to the measurement heights of 30 m, 15 m and 2 m. From left to right: regime F1 to F4, classified based on the 2-m height measurements. The major dashed vertical lines in every panel mark the 1-min scale. Each panel contains box plots representing the distribution of the wT on a corresponding scale. The boxes represent the 25th and 75th percentiles, and the whiskers across the scales are connected with a solid line. The horizontal line in each box shows the median. The statistics are calculated based on all 30-min periods within a flow regime, at the given height. From F1 to F4, there are respectively 401, 489, 86 and 215 individual periods

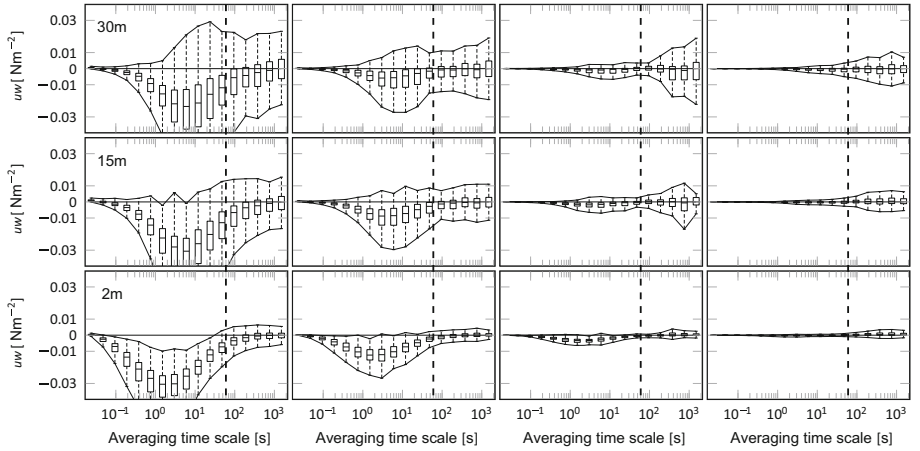

Fig. 4 MRD momentum cospectra of the FLOSSII dataset. The top, middle and bottom rows correspond respectively to the measurement heights of 30 m, 15 m and 2 m. From left to right: regime F1 to F4, classified based on the 2-m height measurements. The major dashed vertical lines in every panel mark the 1-min scale. Each panel contains box plots representing the distribution of the uw on a corresponding scale. The boxes represent the 25th and 75th percentiles, and the whiskers across the scales are connected with a solid line. The horizontal line in each box shows the median. The statistics are calculated based on all 30-min periods within a flow regime, at the given height. From F1 to F4, there are respectively 401, 489, 86 and 215 individual periods

line shows the 1-min average scale as a reference. In all flow regimes, the median MRD shows an increased negative contribution with increasing scales until a maximum, followed by a decrease and finally crossing the zero flux line. This is the signature expected from the

turbulent contribution, and the scale at which the MRD heat flux first reaches zero is typically used to estimate the averaging scale required to sample the turbulent flux.

The multiresolution decompositions of the heat fluxes show that, while the averaged impact of a multitude of submeso-scale contributions to the heat fluxes is very small, individual submeso-scale contributions can be more important to the overall heat flux during a selected 30-min time period than the turbulent contributions. This is apparent from the variability of the submeso-scale range of the MRD, visualized by the interquartile region of the figures at the submeso scales. As the stability increases going from regime S1 to S4 (Fig. 2) or F1 to F4 (Figs. 3, 4), the magnitude of the transport by the turbulent scales reduces, while the variability of the transport by submeso scales (i.e. the interquartile range at those scales) increases. As such, the dynamics becomes more influenced by the submeso scales as stability increases. As the turbulence is collapsing, a state is reached where the magnitude of the heat flux due to sustained turbulent scales is overpassed by the local activity of individual submeso motions (regime S4 and regime F4). In the most stable regimes the local activity of individual submeso motion can be greater than that of the turbulent scales. In individual windows, submeso scales thereby can represent the dominant contribution to the heat transport, although those scales do not systematically contribute to the mean fluxes.

Deeper analyses of the activity and transport properties of different scales of motions in the SnoHATS flow regimes were presented in Vercauteren et al. (2016). Extended MRD analyses suggested a likely direct transfer of energy from the submeso-scale horizontal velocity fluctuations to turbulent vertical velocity fluctuations in regime S3 and S4. Moreover, the analyses suggest that a scale gap separates submeso-scale motions from turbulence in S4, whereas flux variability was found to be more continuous in scale in S3 without a scale gap.

With flow regimes classified according to the interactions between submeso activity and turbulent vertical velocity fluctuations in both datasets, the next section presents the characteristics of submeso motions identified by the TED method in each of the classified flow regimes.

4.3 Characteristics of Events in Different Flow Regimes

Using the window size $l = 120$ points and 6-s averaged data, the first step of the TED method yields 1793 events in the SnoHATS temperature time series obtained by all 12 sonic anemometers, and 702 events in the FLOSSII 2-m temperature time series. A detailed analysis of the events extracted from the 2-m temperature time series of the FLOSSII data is given in Kang et al. (2015), presenting an event clustering approach based on event features that is not repeated here. The physical characteristics of turbulent events are presented here for each of the FEM-BV-VARX flow regimes S1–S4 and F1–F4.

The time series within each regime are discontinuous and the TED method is applied to all continuous portions of the time series individually. Based on a Ri classification, Kang et al. (2015) found that events occurred with similar frequencies for different stability ranges in the FLOSSII dataset. When comparing the frequency of occurrence of events in the flow regimes classified according to their scale-interaction properties, however, differences appear both in the SnoHATS data and in the FLOSSII data (Table 4). In the SnoHATS data, the events account for less than 10 % of the total time in the two regimes identified as weakly influenced by submeso motions and weakly stable (regime S1: 8 % and regime S1: 9 %), whereas events account for 14 % of the total time in regime S3 and 20 % of the total time in regime S4. These two regimes are characterized by a median value of $Ri > 0.25$ (see Table 3). Note that despite the high percentage of events in S4, the percentage of cases where the submeso-scale

Table 4 Frequency of occurrence of the events for the regimes S1–S4 of SnoHATS and F1–F4 of FLOSSII

	SnoHATS/FLOSSII			
	S1/F1	S2/F2	S3/F3	S4/F4
Events [%]	7.5/13.7	9.2/35	14.2/43.4	20.4/38.2

The numbers denote the percentage of the time detected as event within the total time of the corresponding regime

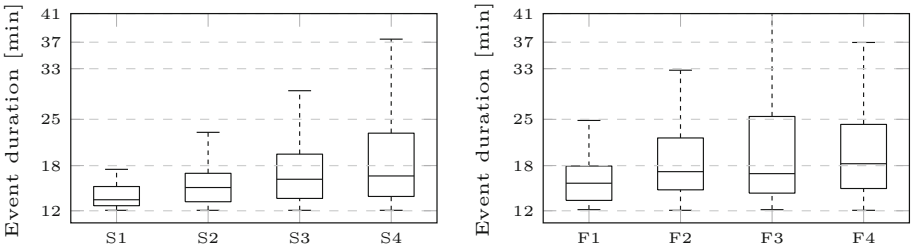

(a) SnoHATS. **(b)** FLOSSII.

Fig. 5 Boxplots of the events duration shown for each FEM-BV-VARX regime separately and for each site

wind speed is higher than the wind speed is smaller in S4 than in S3 (Table 3). Similarly in FLOSSII, the most turbulent regime F1 exhibits the lowest frequency of events (14 %), while the most stable regimes (regime F3 and F4) have the highest frequency of events (above 38 %). A significant difference is, however, found in regime F2 (also weakly stable), in which the frequency of events is large (35 %). It could be that submeso motions are well represented in this regime, but that the mean shear is strong enough for the turbulence to be unaffected by the submeso-scale velocity fluctuations. In fact Vickers and Mahrt (2007) showed that the cross-wind velocity variance due to submeso-scale motions systematically increased with increasing wind speed at the FLOSSII site. This was speculatively attributed to enhanced generation of topographically-induced motions by a nearby ridge, and could partly explain the higher percentage of events for the higher wind-speed regime F3, when compared to the more flat terrain features of the SnoHATS site. Figure 5 further shows the event duration in the four flow regimes found in the SnoHATS and FLOSSII datasets. The event duration increases with increasing regime affiliation number (i.e. with increasing stability and scale interactions) for SnoHATS data, and is not very variable for FLOSSII data except for shorter events in the most turbulent regime F1.

The main physical characteristics of the events found in the different flow regimes are shown in Fig. 6. The statistics of all events occurring in each flow regime are shown for the event-averaged Ri values, for the event-averaged wind speed, for σ_w (where the variance is calculated based on 6-s intervals during the event), and for the event-averaged ratio of submeso-scale wind speed to wind speed. Note that the statistics differ from those given for the flow regimes in Table 3, as they correspond only to TED event periods within a flow regime in Fig. 6. Also shown is the standard deviation of the wind direction during events (based on 6-s intervals to compute the wind direction), and the largest change in temperature and in wind direction during the event (defined as the difference between the maximum and minimum values during the event), so as to detect the signature of microfronts or sharp changes in wind direction. As expected since Regime S1, S2, F1 and F2 correspond to weakly stable periods with little influence of submeso scales on the turbulence, the values of Ri during events are small, the wind speed is relatively high and the vertical velocity fluctuations are large in

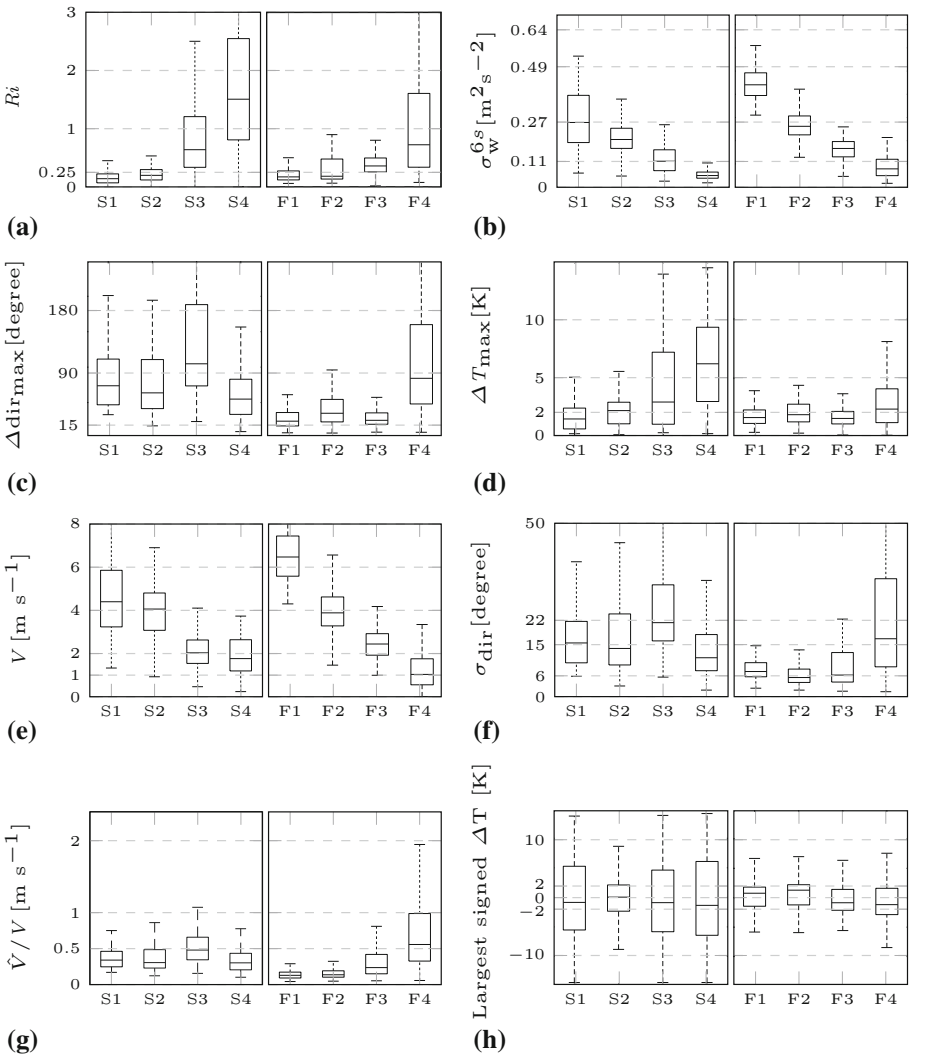

Fig. 6 Boxplots of the TED events physical properties in each flow regime for SnoHATS (S1–S4) and FLOSSII (F1–F4) datasets. The line in each box represents the median over all events in the corresponding flow regime, while the bottom and top of the box are the 25th and 75th percentiles. **a** Richardson number, **b** vertical velocity variance, **c** largest wind-direction change during the event, **d** largest temperature change during the event, **e** mean wind speed, **f** standard deviation of the wind direction, **g** submeso-scale to mean-wind ratio, **h** largest signed temperature change during the event. In panels **a**, **b**, **e**, **f**, **g**, the values for individual TED events are calculated as the mean over the duration of the event, and a 6-s averaging interval is used for variance and standard deviation calculations. In panels **c**, **d**, **h**, the largest change refers to the maximum difference between two consecutive 6-s intervals during the event

those regimes. The vertical velocity fluctuations decrease with increasing regime affiliation number, corresponding to increasing stability and modulation by the submeso-scale wind speed. Events in regimes S4 and F4 are associated with small turbulent vertical velocity fluctuations only.

The largest differences appear in the behaviour of the wind direction, of the temperature and of the submeso-scale to mean wind-speed ratio during events, in the most stable regimes. Events in regime S3 have a very large wind-direction variability in SnoHATS data and a slightly larger variability in F3 when compared to F1 and F2 for FLOSSII data. In regimes S4 and F4, both characterized by a median $Ri > 0.6$, the datasets differ markedly. The events of FLOSSII data have a very large directional variability and large directional shifts. Such directional shifts were in fact shown to be common in the SBL for low wind speeds by Mahrt (2010), based on the FLOSSII data. In the latter study, the strongest wind-direction shifts were shown to occur often with a sharp decrease of temperature (a cold microfront). This was also found by Lang et al. (2018) over a flat site in Australia. Moreover, Mahrt et al. (2012b) attributed an observed increase of wind-directional shear at the FLOSSII site for increasing stratification during the advection of cold air due to a cold pool forming upwind of the site. This is consistent with the events statistics for regime F4, where the events are characterized by the largest wind-directional shifts as well as the largest temperature changes, which are mostly negative (panels c, d and h). They are also characterized by the largest $\hat{V}/V$ ratios, which together with the wind-directional variability are a sign of wave-like activity. The events in the SnoHATS dataset, however, behave differently. Events in regime S3 show signs of wave-like or advection activity similar to those seen in F4, with correspondingly larger $\hat{V}/V$. The temperature changes are larger in regime S4 than in regime S3, however regime S4 has the least wind-direction variability. In fact, analysis of the wind-direction distribution during events in regime S4 point to a preferred direction pointing straight towards the instruments. This direction corresponds to an opening at the end of the glacier, forming a funnel that probably induces a wind direction constrained by the topography (Fig. 1). The statistics in Fig. 6h highlight a majority of temperature changes related to cold microfronts. The cold-microfront events correspond to small vertical velocity variance, and to rather small $\hat{V}/V$. This could indicate a regime where decreasing turbulence, surface cooling and increasing stratification evolve together. The flow is near-calm and wave-like activity is no longer present. A similar regime is not detected in the FLOSSII dataset.

Regime S4 is thus characterized by submeso motions on scales significantly larger than the turbulent scales (as is better highlighted by analyses in Vercauteren et al. 2016), which take a slow microfront signature with little wind-direction variability. We hypothesise that advected airmasses or density currents that tend to take a microfront structure, while enhancing shear locally, may trigger only minimal turbulence on small scales. Regime F4 has a similar scale signature and microfronts structures, but the site features are such that the microfronts also correspond to large shifts in the wind direction. Nevertheless, these events also trigger only minor turbulent mixing. On the contrary, the wind-direction variability characteristics of events in regime S3, with its scale overlap that was identified in Vercauteren et al. (2016), lead us to hypothesise that this regime encompasses wave-like phenomena that may break down to turbulence through a cascade of scales. The submeso-scale wind speed in this regime is often larger than the mean wind speed.

4.4 Example of Events and Flow Structures

The events were detected by the TED method based solely on the temperature time series, without considering information on the wind direction. In this section we explore the flow structures corresponding to selected events, taken as examples in each identified flow regime. One example of such an event is shown for each flow regime for SnoHATS data in Fig. 7, and for each flow regime for FLOSSII data in Fig. 8. Examples are chosen that approxi-

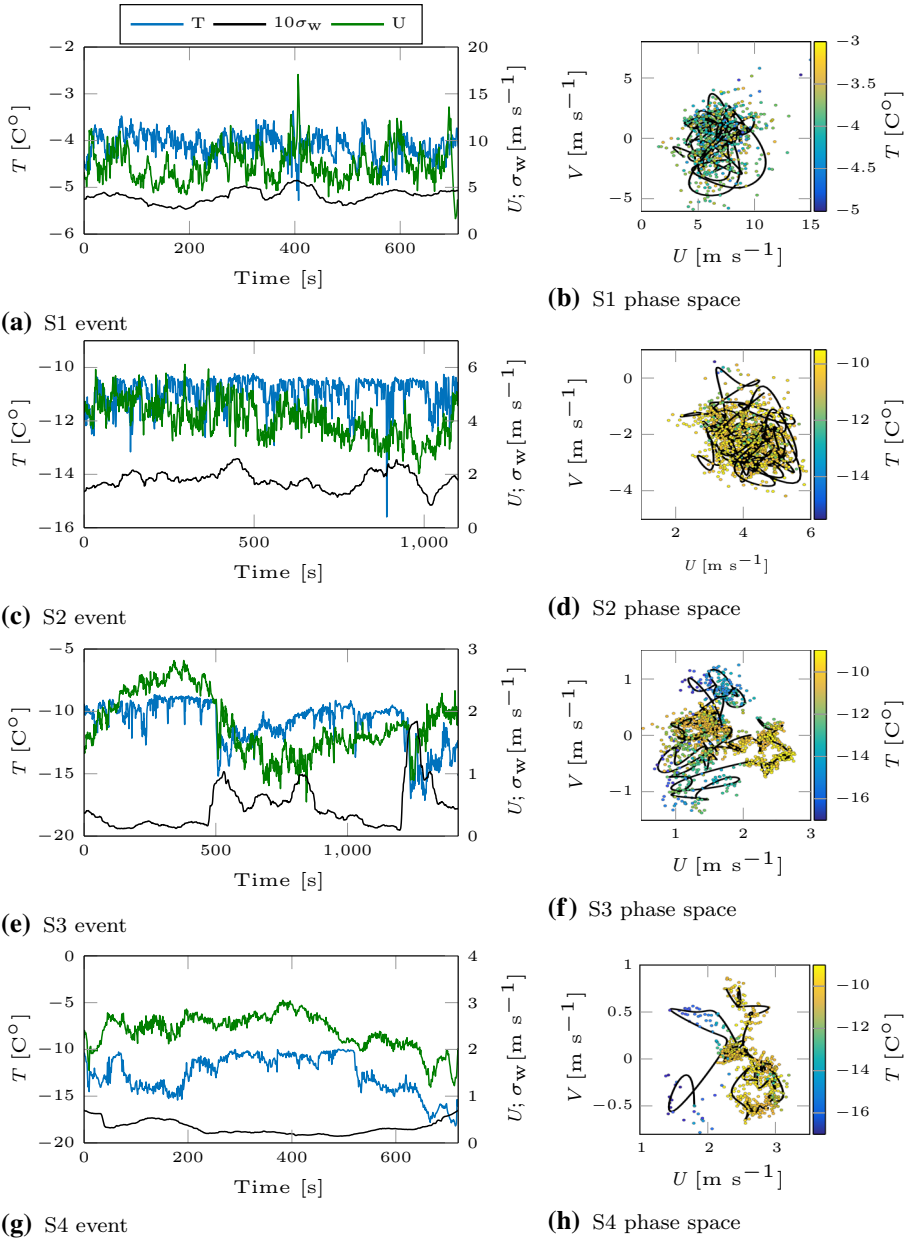

Fig. 7 Visualization of turbulent events for the SnoHATS dataset. One event is shown as an example for each regime. The time series on the left show the temperature T (blue), the wind speed U (green) and the vertical velocity component w (black), all shown for 6-s averaged data. The scatterplots show the temperature in colour, in the phase space of the horizontal velocity components. The black line is a spline smoothing of the time evolution of the wind vector

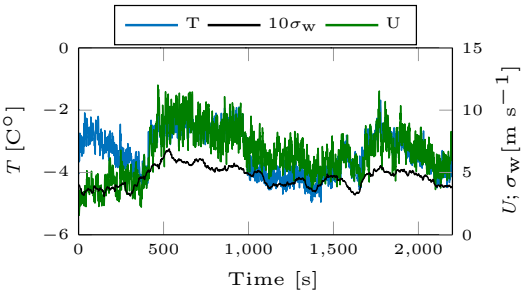

(a) F1 event

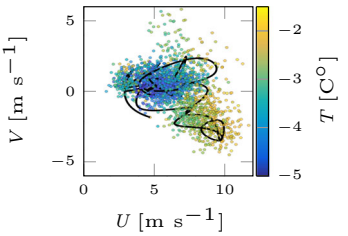

(b) F1 phase space

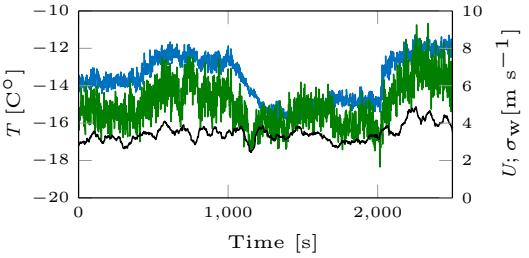

(c) F2 event

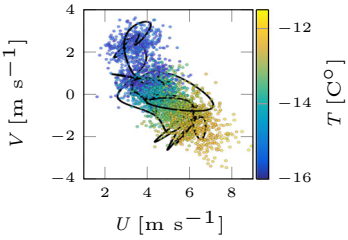

(d) F2 phase space

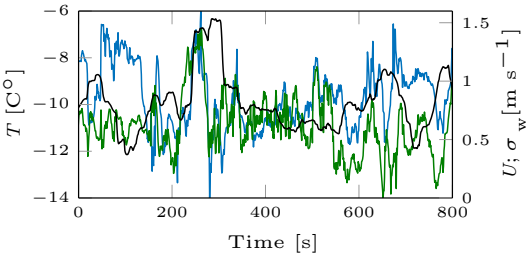

(e) F3 event

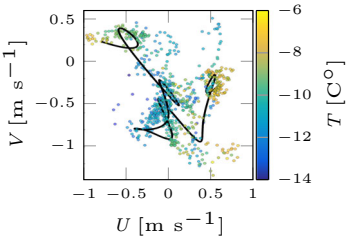

(f) F3 phase space

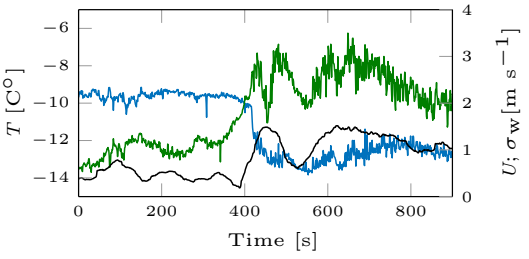

(g) F4 event

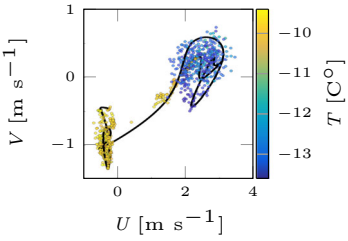

(h) F4 phase space

Fig. 8 Visualization of turbulent events for the FLOSSII dataset. One event extracted from the 2-m measurement height is shown as an example for each regime. The time series on the left show the temperature T (blue), the wind speed U (green) and the vertical velocity component w (black), all shown for 6-s averaged data. The scatterplots show the temperature in colour, in the phase space of the horizontal velocity components. The black line is a spline smoothing of the time evolution of the wind vector

mately match the median characteristics illustrated in Fig. 6. The selection was done after visual analysis of all events, based on what appeared to be the most frequent or typical examples (additionally to matching the median characteristics approximately). In the examples selected from S1 and S2, the time series of temperature T and wind speed U show an oscillating behaviour that is not followed by σ_w (Fig. 7a, c), as was observed by the FEM-BV-VARX clustering results (see Table 2). The corresponding evolution of the horizontal velocity components during the events is shown in Fig. 7b, d, where the corresponding evolution of the temperature is represented by the colours in the scatterplot. The black line in the scatterplots is a smoothing of the time evolution of the wind vector, so as to smooth out the turbulence variability. This visualization of the event highlights rather a mixing process, with no clear pattern in the temperature distribution (Fig. 7b, d). The time series of temperature T, wind speed U and σ_w for the events in F1 (Fig. 8a) and F2 (Fig. 8c) show that T and U tend to evolve in phase with a wavy pattern, but that σ_w does not follow the dynamics of T and U. This is in agreement with what was observed from the FEM-BV-VARX clustering analysis, where no relationship was found between σ_w and the time evolution of the submeso-scale wind speed (see Table 2). In Fig. 8b, d, the wind vector evolves in a compact structure, and the temperature changes smoothly following the wind vector. In these weakly stable regimes, events are present but σ_w remains rather stationary during the events. The events for FLOSSII are more structured in phase space than for SnoHATS, which could be related to the differences in terrain complexity as discussed above.

In Sect. 4.3 we pointed out that sharp temperature changes in time occur in the most stable flow regimes S3-S4 and F4 (see Fig. 6d), being geatest in S4 and F4, while wind-direction changes have a more site-specific signature (see Fig. 6c). The wind-direction variability during events is largest in S3, F3 and F4 and is visible in the examples from F3 and F4, both highlighting a dispatched structure in the time evolution of the wind vector (Fig. 8f). The example of F4 has a sharp change of wind direction that is simultaneous with the sharp change of temperature (8h). This is the typical signature of a microfront that is commonly found with weak winds and a thin stable boundary layer (Mahrt 2010; Lang et al. 2018). For both examples, the dynamical evolution of σ_w is highly non-stationary, partly affected by the evolution of T and U (Fig. 8e, g). In the example from S3, the time evolution of the wind direction seen in the phase-space figure has a clear structure, but denotes less sharp transitions in wind direction than in the FLOSSII examples (Fig 7f). The drop in temperature occurs sharply, with only a slight change in wind direction (visible in phase space as the transition from the homogeneous temperature part of the scatterplot on the right side to the left side of the scatterplot). Increases in σ_w occur simultaneously with decreases in the temperature (Fig. 7e), and the evolution of T and U is approximately in phase. In the example of S4, however, σ_w seems rather stationary again, and the decrease in temperature and wind speed does not correspond to a marked increase of σ_w (Fig. 7g), the wind direction is oscillating (Fig. 7h). This example may correspond to the radiative regime suggested in van de Wiel and Moene (2003), with flow meandering but a collapsed state of turbulence.

These examples are just a few of many events for which no clear dominant patterns are apparent. Regularity of event signatures was searched for using the clustering method suggested in Kang et al. (2015), which highlighted recurring event signatures in the FLOSSII dataset. For the SnoHATS dataset, however, similar regularity was not made apparent through that clustering approach, and did not appear after visual inspection either. The classes of submeso-scale and turbulence interaction analyzed herein identify different regimes which may have a preference for the existence or absence of temperature microfronts, sharp changes in wind direction or wind oscillations. However, the specific types of submeso motions occurring may be more dependent on the local terrain features and less on the flow type. We

expect flow regimes with active turbulence to quickly dissipate submeso motions, whereas quieter regimes allow such flow structures to be transported for a longer time and thereby to affect the turbulence to some extent. This picture is consistent with the hypothesis of a dynamically unstable flow in a transition zone near a critical wind speed separating two distinct metastable flow equilibria (one with active turbulence and the other with collapsed turbulence), suggested by the conceptual model of van de Wiel et al. (2017). Indeed, in the transition zone near the critical wind speed, the response time of the flow to perturbations becomes large, such that random perturbations of the flow by submeso motions are long-lived. This is in agreement with the statistical analyses presented in Nevo et al. (2017), who suggested that the more stable regimes are dynamically unstable, based on analyzing memory effects in time series of turbulent observed variables in the different flow regimes.

5 Conclusion

Flow regimes were classified in terms of interactions between submeso and turbulent scales of motion. In each flow regime, turbulent events were extracted using the turbulent event detection method, and the statistical properties of those events were characterized. Regimes experiencing little scale interactions (S1, S2, F1, F2) are characterized by the shortest events, higher wind speeds, weak stability and fewer events.

Regimes experiencing greater scale interactions correspond to higher stability, more numerous and longer events. In the most stable regimes that occur with weak winds, with a scale separation between turbulent and submeso scales, the signature of events was found to take a site specific signature, probably related to local topographical characteristics. Events in these very weak wind conditions tend to exhibit strong temperature changes, with wind-direction variability characteristics that depend on the site, probably through the terrain specificities. The site differences exemplified here in two datasets render the derivation of parametrizations difficult. These flow regimes could be related to radiative cooling, advected airmasses, density currents, and events thus tend to take a microfront structure with sharp temperature changes. Local shear enhancement due to the advected airmasses results in turbulent mixing as identified by the FEM-BV-VARX method but the turbulent mixing occurs on very local, small scales. There may be a direct energy transfer between submeso scales and turbulent scales through the local shear generation of small-scale eddies, as was analyzed in Vercauteren et al. (2016).

In regimes where the submeso-scale wind speed is often larger than the wind speed (S3, F3), or where the submeso and turbulent scales tend to overlap (S3), events are characterized by a large variability in the wind direction during the selected event. Temperature changes are, however, less sharp than in the most stable regimes S4 or F4 in which turbulence is nearly collapsed. Events are associated with stronger vertical-velocity fluctuations than in the very weak-wind, strongly stable regimes S4 and F4. This could potentially be more related to wave-like phenomena that break down to turbulence through a cascade of scales.

The multiresolution flux-decompostion analyses point to the randomness of submeso-scale contributions. The averaged contribution of the submeso scales to the heat flux is negligible, however individual contributions become larger than turbulent contributions in strongly stable, weak-wind regimes. The phenomena leading to the submeso-scale motions and associated fluxes are not resolved nor taken into account in numerical models, except through artificial enhanced mixing. The combination of flow regime detection to extract periods where submeso motions tend to dominate over turbulent transport and characterization

of events in each regime provides a means of defining a stochastic process based on the statistical analyses. More extensive analyses based on machine-learning methods, for example using neural network methods to identify patterns using all the observables corresponding to events, may help shed light on the regularity of submeso motions.

Acknowledgements The authors thank Marc Parlange and the EFLUM laboratory at EPFL for providing the SnoHATS data and Larry Mahrt for providing the FLOSSII data and help to analyze them. Illia Horenko and Dimitri Igdalov provided the FEM-BV-VARX framework and help that was greatly appreciated. Alexander Kuhn is greatly acknowledged for his software provided to visualise flow structures. The research was funded by the Deutsche Forschungsgemeinschaft (DFG) through grant number VE 933/2-1 "Towards Stochastic Modelling of Turbulence in the Stable Atmospheric Boundary Layer", and has been partially supported by the DFG through the CRC 1114 "Scaling Cascades in Complex Systems", Project (B07) "Selfsimilar structures in turbulent flows and the construction of LES closures".

References

Acevedo OC, Mahrt L, Puhales FS, Costa FD, Medeiros LE, Degrazia GA (2015) Contrasting structures between the decoupled and coupled states of the stable boundary layer. Q J R Meteorol Soc 142(695):693–702

Anfossi D, Oettl D, Degrazia G, Goulart A (2005) An analysis of sonic anemometer observations in low wind speed conditions. Boundary-Layer Meteorol 114(1):179–203

Belušić D, Güttler I (2010) Can mesoscale models reproduce meandering motions? Q J R Meteorol Soc 136(648):553–565

Bou-Zeid E, Higgins CW, Huwald H, Meneveau C, Parlange M (2010) Field study of the dynamics and modelling of subgrid-scale turbulence in a stable atmospheric surface layer over a glacier. J Fluid Mech 665:480–515

Brockwell PJ, Davis RA (2002) Introduction to time series and forecasting, 2nd edn. Springer, Berlin

Cava D, Mortarini L, Giostra U, Richiardone R, Anfossi D (2016) A wavelet analysis of low-wind-speed submeso motions in a nocturnal boundary layer. Q J R Meteorol Soc 143(703):661–669

Donda JMM, van Hooijdonk IGS, Moene AF, Jonker HJJ, van Heijst GJF, Clercx HJH, van de Wiel BJH (2015) Collapse of turbulence in stably stratified channel flow: a transient phenomenon. Q J R Meteorol Soc 141(691):2137–2147

Faranda D, Pons FME, Dubrulle B, Daviaud F, Saint-Michel B, Herbert É, Cortet PP (2014) Modelling and analysis of turbulent datasets using ARMA processes. Phys Fluids (1994-present) 10:101–105

Horenko I (2010) On the identification of nonstationary factor models and their application to atmospheric data analysis. J Atmos Sci 67(5):1559–1574

Kaiser A (2016) Stably stratified atmospheric boundary layers: event detection and classification for turbulent time series. Bachelor thesis, Freie Universität Berlin

Kang Y, Belušić D, Smith-Miles K (2014) Detecting and classifying events in noisy time series. J Atmos Sci 71(3):1090–1104

Kang Y, Belušić D, Smith-Miles K (2015) Classes of structures in the stable atmospheric boundary layer. Q J R Meteorol Soc 141(691):2057–2069

Kolmogorov AN (1941) The local structure of turbulence in incompressible viscous fluid for very large Reynolds numbers. Dokl Akad Nauk SSSR 30:299

Lang F, Belušić D, Siems S (2018) Observations of wind-direction variability in the nocturnal boundary layer. Boundary-Layer Meteorol 166(1):51–69. https://doi.org/10.1007/s10546-017-0296-4

Lilly JM (2017) Element analysis: a wavelet-based method for analysing time-localized events in noisy time series. Proc R Soc A 473(2200):20160–776

Mahrt L (2010) Common microfronts and other solitary events in the nocturnal boundary layer. Q J R Meteorol Soc 136(652):1712–1722

Mahrt L (2014) Stably stratified atmospheric boundary layers. Annu Rev Fluid Mech 46:23–45

Mahrt L, Thomas CK (2016) Surface stress with non-stationary weak winds and stable stratification. Boundary-Layer Meteorol 159(1):3–21

Mahrt L, Richardson SJ, Seaman N, Stauffer DR (2012a) Turbulence in the nocturnal boundary layer with light and variable winds. Q J R Meteorol Soc 138(667):1430–1439

Mahrt L, Thomas CK, Richardson SJ, Seaman N, Stauffer DR, Zeeman MJ (2012b) Non-stationary generation of weak turbulence for very stable and weak-wind conditions. Boundary-Layer Meteorol 147(2):179–199

Mortarini L, Cava D, Giostra U, Acevedo OC, Nogueira Martins LG, Soares de Oliveira PE, Anfossi D (2017) Observations of submeso motions and intermittent turbulent mixing across a low level jet with a 132-m tower. Q J R Meteorol Soc 144(710):172–183

Nevo G, Vercauteren N, Kaiser A, Dubrulle B, Faranda D (2017) Statistical-mechanical approach to study the hydrodynamic stability of the stably stratified atmospheric boundary layer. Phys Rev Fluids 2(8):084–603

Obukhov AM (1941) On the distribution of energy in the spectrum of turbulent flow. Dokl. Akad. Nauk SSSR 32:19

O'Kane TJ, Risbey JS, Franzke C, Horenko I, Monselesan DP (2013) Changes in the metastability of the midlatitude southern hemisphere circulation and the utility of nonstationary cluster analysis and split-flow blocking indices as diagnostic tools. J Atmos Sci 70(3):824–842

O'Kane TJ, Risbey JS, Monselesan DP, Horenko I, Franzke CLE (2016) On the dynamics of persistent states and their secular trends in the waveguides of the Southern Hemisphere troposphere. Clim Dyn 46(11–12):3567–3597

Pope SB (2000) Turbulent flows. Cambridge University Press, Cambridge

Román Cascón C, Yagüe C, Mahrt L, Sastre M, Steeneveld GJ, Pardyjak E, van de Boer A, Hartogensis O (2015) Interactions among drainage flows, gravity waves and turbulence: a BLLAST case study. Atmos Chem Phys 15(15):9031–9047

Sandu I, Beljaars ACM, Bechtold P, Mauritsen T, Balsamo G (2013) Why is it so difficult to represent stably stratified conditions in numerical weather prediction (NWP) models? J Adv Model Earth Syst 5(2):117–133

Sun J, Lenschow DH, Burns S, Banta RM, Newsom R, Coulter R, Nappo CJ, Frasier S, Ince T, Balsley BB (2004) Atmospheric disturbances that generate intermittent turbulence in nocturnal boundary layers. Boundary-Layer Meteorol 110(2):255–279

Sun J, Mahrt L, Banta RM, Pichugina YL (2012) Turbulence regimes and turbulence intermittency in the stable boundary layer during CASES-99. J Atmos Sci 69(1):338–351

Sun J, Mahrt L, Nappo CJ, Lenschow DH (2015) Wind and temperature oscillations generated by wave-turbulence interactions in the stably stratified boundary layer. J Atmos Sci 72(4):1484–1503

Thomson DJ (1987) Criteria for the selection of stochastic models of particle trajectories in turbulent flows. J Fluid Mech 180(–1):529–556

van de Wiel BJH, Moene AF (2003) Intermittent turbulence in the stable boundary layer over land. Part III: a classification for observations during CASES-99. J Atmos Sci 60(20):2509–2522

van de Wiel BJH, Moene AF, Jonker HJJ (2012a) The cessation of continuous turbulence as precursor of the very stable nocturnal boundary layer. J Atmos Sci 69:3097–3115. https://doi.org/10.1175/JAS-D-12-064.1

van de Wiel BJH, Moene AF, Jonker HJJ, Baas P, Basu S, Donda JMM, Sun J, Holtslag A (2012b) The minimum wind speed for sustainable turbulence in the nocturnal boundary layer. J Atmos Sci 69(11):3116–3127

van de Wiel BJH, Vignon E, Baas P, van Hooijdonk IGS, van der Linden SJA, Antoon van Hooft J, Bosveld FC, de Roode SR, Moene AF, Genthon C (2017) Regime transitions in near-surface temperature inversions: a conceptual model. J Atmos Sci 74(4):1057–1073

van Hooijdonk IGS, Donda JMM, Clercx HJH, Bosveld FC, van de Wiel BJH (2015) Shear capacity as prognostic for nocturnal boundary layer regimes. J Atmos Sci 72(4):1518–1532

Vercauteren N, Klein R (2015) A clustering method to characterize intermittent bursts of turbulence and interaction with submesomotions in the stable boundary layer. J Atmos Sci 72(4):1504–1517

Vercauteren N, Mahrt L, Klein R (2016) Investigation of interactions between scales of motion in the stable boundary layer. Q J R Meteorol Soc 142(699):2424–2433

Vercauteren N, Boyko V, Faranda D, Stiperski I (2019) Scale interactions and anisotropy in stable boundary layers. Q J R Meteorol Soc. https://doi.org/10.1002/qj.3524

Vickers D, Mahrt L (2003) The cospectral gap and turbulent flux calculations. J Atmos Ocean Technol 20(5):660–672

Vickers D, Mahrt L (2007) Observations of the cross-wind velocity variance in the stable boundary layer. Environ Fluid Mech 7(1):55–71

Zeeman MJ, Selker JS, Thomas CK (2014) Near-surface motion in the nocturnal, stable boundary layer observed with fibre-optic distributed temperature sensing. Boundary-Layer Meteorol 154(2):189–205